

Microstructure and High-Temperature Tribological Properties of Laser-Cladded WC10Co4Cr–xTi₂AlC Coatings



XI HUI and KONG DEJUN

To enhance the tribological performance of ceramic coatings, the Ti₂AlC phase was used as reinforcement to WC10Co4Cr coating by laser cladding. The microstructure and phases of obtained coatings were analyzed using a super-depth field microscope and X-ray diffraction, respectively. The effects of Ti₂AlC mass fraction on the tribological properties of WC10Co4Cr–xTi₂AlC coatings at 500 °C were investigated using a high-temperature wear tester, and the wear mechanism was also discussed in detail. The results demonstrate that the hardness of WC10Co4Cr–0, – 5, – 10 and – 15 pct Ti₂AlC coatings is 1156 ± 57 , 1514 ± 75 , 1423 ± 71 , and 1354 ± 67 HV_{0.5}, respectively, showing that the WC10Co4Cr–5 pct Ti₂AlC coating have the highest hardness among the four kinds of coatings. The average coefficients of friction of WC10Co4Cr–0, – 5, – 10, and – 15 pct Ti₂AlC coatings is 0.828, 0.419, 0.591, and 0.738, respectively, and the corresponding wear rates are 55.85, 22.71, 34.05, and 39.33 $\mu\text{m}^3 \text{N}^{-1} \text{mm}^{-1}$, respectively. The wear mechanism of WC10Co4Cr–xTi₂AlC coatings is abrasive wear, fatigue wear, adhesive wear, and oxidative wear, in which the appropriate Ti₂AlC mass fraction plays the role of wear resistance in the friction process.

<https://doi.org/10.1007/s11661-024-07373-0>

© The Minerals, Metals & Materials Society and ASM International 2024

I. INTRODUCTION

IN recent years, surface coatings have been used to improve the wear resistance of H13 steel, mainly including physical vapor deposition (PVD), plasma spraying, laser cladding (LC), *etc.*^[1–5] In particular, LC may deposit ceramic coatings on the metal substrate^[6] with many advantages such as high forming efficiency, controllable quality, and low dilution rate.^[7,8]

Among numerous coatings, tungsten carbide (WC) with high hardness^[9,10] has great potential in the coating field. Ma *et al.*^[11] found that the WC–12Co had favorable characteristics with the low porosity and high bonding strength of 44 MPa, which was a promising candidate for the improvement of wear resistance on the coatings at high-temperature conditions. Liu *et al.*^[12] fabricated the WC to reinforce CuNiMn coatings and found that the uniform distribution of WC was attributed to the increase in wear resistance. Wang *et al.*^[13] investigated the size of WC particles on the influence on the wear resistance of WC–Co coating and

revealed that the reduction of WC particle size led to a decrease in wear rate. Moreover, Wang *et al.* also elucidated that the WC particles were easily deposited on the coating bottom, where existed some pores and cracks.^[14]

Currently, MAX ceramic phases are used to improve the microstructure of ceramic coatings, and their basic chemical formula is represented as $M_{n+1}AX_n$, where M , A , and X represent the transition metal element, main group element, and carbon or nitrogen, respectively.^[15,16] Most of the discovered MAX phases are H-phase, such as Ti₂AlC and Cr₂AlC, which have unique nanolayered structures and both metallic and ceramic characteristics.^[17] Especially, the Ti₂AlC has a ternary layered structure, where TiC and AlC are served as interlayer fillers. Its hexagonal close-packing (HCP) crystal structure is similar to that of diamond, but Al atoms replace the Ti atoms partially, resulting in the alternative arrangement of Ti and Al atoms. The special layered and hierarchical structures impart Ti₂AlC series of unique properties, mainly including self-lubrication, high toughness, and high-temperature stability.^[15,18] Moreover, Ti₂AlC also has a unique layered structure to enhance coating crack-healing ability,^[19,20] which has the potential to decompose and synthesize the hard phase.^[21]

In this study, Ti₂AlC particles were added to the WC10Co4Cr coating to reduce the coating cracks and improve its wear resistance. The objective was to investigate the influence of Ti₂AlC mass fraction on

XI HUI and KONG DEJUN are with the School of Mechanical Engineering, Changzhou University, Changzhou 213164, P.R. China. Contact e-mail: kong-dejun@163.com

Manuscript submitted September 28, 2023; accepted March 10, 2024.

Article published online March 24, 2024

the tribological properties of WC10Co4Cr- x Ti₂AlC coatings at high-temperature, and the wear mechanism of WC10Co4Cr- x Ti₂AlC coatings was also discussed, which provided an approach for the modification treatment of WC10Co4Cr coating.

II. EXPERIMENTAL PROCEDURES

A. Coating Preparations

The substrate was H13 steel for the LC, and the WC10Co4Cr powder with the size of 15 to 45 μm was used as the LC main material. The respective mass fraction of 5, 10, and 15 pct Ti₂AlC powder was added to WC10Co4Cr powder, which was mixed in a QM-3SP04L planetary ball miller. The process parameters were shown as follows: rotational speed of 500 rpm; ZrO₂ ball diameter of 6 mm; and operation time of 120 minutes. The morphologies of WC10Co4Cr and Ti₂AlC powders were observed using a JSM-6510 type scanning electron microscope (SEM), as shown in Figures 1(a) and (b), respectively. The WC10Co4Cr and Ti₂AlC powder were mainly spherical and regular polygons, respectively, which were suitable for the LC process. The XRD analysis of WC10Co4Cr- x Ti₂AlC powders were analyzed using a D/max 2500PC X-ray diffraction (XRD) with the Cu-K α radiation (λ 1.5406 Å), as shown in Figure 1(c). All the WC10Co4Cr- x Ti₂AlC coatings were composed of WC, TiC, Ti₂AlC, and eutectic carbide phase of η -Co (Co₃W₃C).^[22]

The LC process was carried out on an RFL-C3300W type fiber machine with the transverse powder feeding method. The LC parameters were shown as follows: spot diameter of 4 mm; laser power of 1700 W; scanning speed of 7 mm/s; powder feeding speed of 12 g/s; argon flow of 5 L/min; and overlap rate of 50 pct.

B. Characterization Methods

After the LC experiment, the obtained coatings were cut into the dimensions of 15 \times 15 \times 5 mm³ and their surfaces and cross-sections were ground with #80-2000 SiC sandpaper and polished with 0.5 μm diamond polishing compound. Subsequently, the coatings were corroded with 5 pct FeCl₃ solution to observe the optical microscope (OM) images on a VHX-700F type super-depth field microscope (SDFM), and the phase was analyzed using a D/max2500PC type XRD. The porosity of the obtained coating surfaces was measured with the Image-J software. The hardness of coating surfaces and cross-sections was measured using an HVS-1000 M type Vickers microhardness tester, and the test parameters were shown as follows: load of 5 N; and holding time of 10 seconds.

C. Frictional Wear Test

The high-temperature friction test was conducted on an HT-1000 type high-temperature friction tester, as shown in Figure 1(d), in which the coefficients of friction (COFs) were recorded real-time by the computer

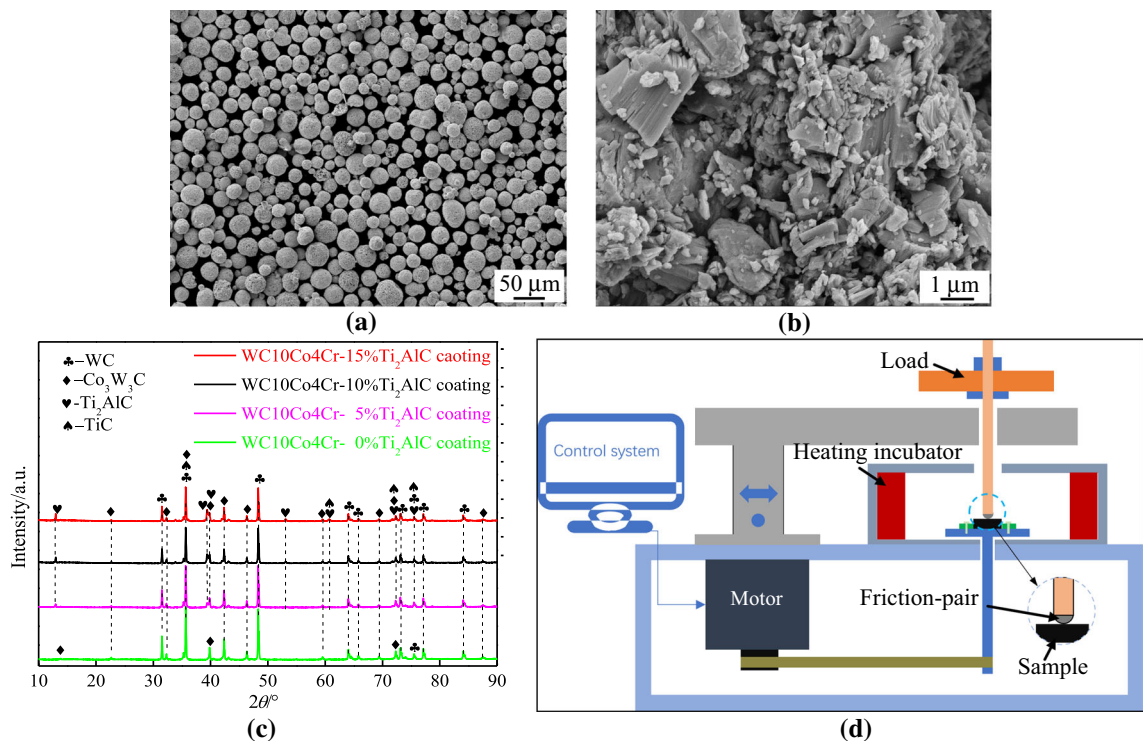


Fig. 1—Morphologies of WC10Co4Cr (a) and Ti₂AlC powders (b), XRD analysis of WC10Co4Cr- x Ti₂AlC powders (c) and diagram of friction test (d).

system.^[23] The test parameters were shown as follows: friction-pair of Si₃N₄ ball with a diameter of 5 mm; normal load of 5 N; motor frequency of 8.93 Hz; rotational speed of 500 rpm; rotation radius of 2 mm; and wear time of 30 minutes. After the friction test, the profiles of wear tracks were measured on SDFM, and the profile areas were calculated using the Origine-2018 software.

In this case, the wear rate was^[24]

$$W = \frac{V}{F \times S} \quad [1]$$

where V was the wear volume (μm^3); F was the normal load (N); and S was the total sliding length (mm).

The wear volume in Eq. [2] was^[25]

$$V = 2\pi r \times A \quad [2]$$

where r was the rotation radius (mm); and A was the profile area of the wear track measured by the SDFM and calculated by the original software (mm^2).

III. ANALYSIS AND DISCUSSION

A. Characteristics of Coatings

1. OM images and porosity of coating surfaces

Figure 2(a) displays the OM image and porosity of WC10Co4Cr-0 pct Ti₂AlC coating. The coating surface mainly consisted of WC particles, which exhibited triangular and polygonal shapes.^[25] In the enlarged image, it could be seen that there were black pores on the WC10Co4Cr-0 pct Ti₂AlC coating surface.

Figures 2(b) through (d) displays the OM images and porosities of WC10Co4Cr-5 pct Ti₂AlC, -10 pct Ti₂AlC and -15 pct Ti₂AlC coatings. All the WC10Co4Cr- x -Ti₂AlC coating surfaces were smooth, and the Ti₂AlC suppressed the grain growth of the CoCr binder, resulting in a decrease in grain sizes. Therefore, the coating grains became fined compared with the WC10Co4Cr-0 pct Ti₂AlC coating and the sharp edges of hard phases became smooth. The grain sizes of WC10Co4Cr- x -Ti₂AlC coatings increased with the Ti₂AlC mass fraction, and some special structures became visible, which presented as dendritic form as the Ti₂AlC mass fraction increased. Moreover, the addition of Ti₂AlC presented the ability to reduce the formation of cracks, which was closely linked to the self-healing properties at high temperatures.^[26] Figure 2(e) shows the grain sizes of WC10Co4Cr- x -Ti₂AlC coatings. The average grain diameters of WC10Co4Cr-5 pct Ti₂AlC, -10 pct Ti₂AlC, and -15 pct Ti₂AlC coatings were 7.7, 11.8, and 15.2 μm , respectively, which were lower than 23.4 μm of WC10Co4Cr coating. As a result, the grains of WC10Co4Cr- x -Ti₂AlC coatings were refined by the addition of Ti₂AlC, and the WC10Co4Cr-5 pct Ti₂AlC had the smallest grain size, which benefited from improving the coating hardness.

Figures 2(a) through (d) also shows the porosity of WC10Co4Cr- x -Ti₂AlC coating surfaces, in which the

porosity was defined as the ratio of pore volume and total volume.^[27,28] In this case, the porosity of WC10Co4Cr- x -Ti₂AlC coating surfaces was calculated from the OM images. The white spots represented pores in the images. The results showed that the porosity of WC10Co4Cr-5, -10, and -15 pct Ti₂AlC coating surfaces was 0.70, 1.10, and 1.81 pct, respectively, which was lower than 2.31 pct of WC10Co4Cr-0 pct Ti₂AlC coating.

2. OM images of coating cross-sections

Figure 3(a) shows the OM images of WC10Co4Cr-0 pct Ti₂AlC coating cross-sections, which exhibited semi-circular and multi-pass metallurgical bonding with the substrate at the fusion boundary.^[29] This was because the energy density at the center of the laser spot was higher and produced a higher heat in the middle region compared with the sides, which caused the substrate to melt faster and deeper.^[30] In this case, the cross-section showed crack defects, and there were some pores, which was because the residual gas in the coatings led to the pore formation.

Figures 3(b) through (d) shows the OM images of WC10Co4Cr-5, -10 and -15 pct Ti₂AlC coating cross-sections. The thicknesses of WC10Co4Cr-5, -10, and -15 pct Ti₂AlC coatings were 1061, 1121, and 1138 μm , respectively, which had a smooth interface with the fusion boundary of a substrate. However, the white defects appeared on the cross-sections as the Ti₂AlC mass fraction increased, which was the dissolution of excessive Ti₂AlC. In this case, the WC10Co4Cr- x -Ti₂AlC coatings showed better metallurgical bonding compared with the WC10Co4Cr-0 pct Ti₂AlC coating,^[31,32] and there was no evident cracking on the coating cross-sections.

B. XRD Analysis

Figure 4 shows the XRD analysis of WC10Co4Cr- x -Ti₂AlC coatings. The WC10Co4Cr-0 pct Ti₂AlC coating was composed of WC, W₂C, η -Co (Co₃W₃C), Fe₃W₃C, and Co Cr phases, in which the sharp peak indicated the crystal structure.^[33] The appearances of peaks on the WC10Co4Cr- x -Ti₂AlC coatings were attributed to the formations of phases such as W₂C, Fe₃W₃C, Ti₂AlC, and CoO, in which the intensity of WC was decreased. All the WC10Co4Cr- x -Ti₂AlC coatings were composed of multiple phases, which led to the structural evolution. The W₂C content increased with the Ti₂AlC mass fraction, where the W₂C was the product of WC decarburization.^[34,35] However, the intensity of W₂C peak decreased as the Ti₂AlC mass fraction increased, showing an inverse relationship. This was because the ordering of crystal structure decreased, which caused the peak intensity decrease. Furthermore, the W₂C peak at 36.4 deg became wide, indicating that the addition of Ti₂AlC affected grain refinement. During the LC process, the Co also reacted with the O to form CoO, which further enhanced the oxidation resistance of WC10Co4Cr- x -Ti₂AlC coatings. The formations of W₂C and CoO in the LC process were shown as follows:

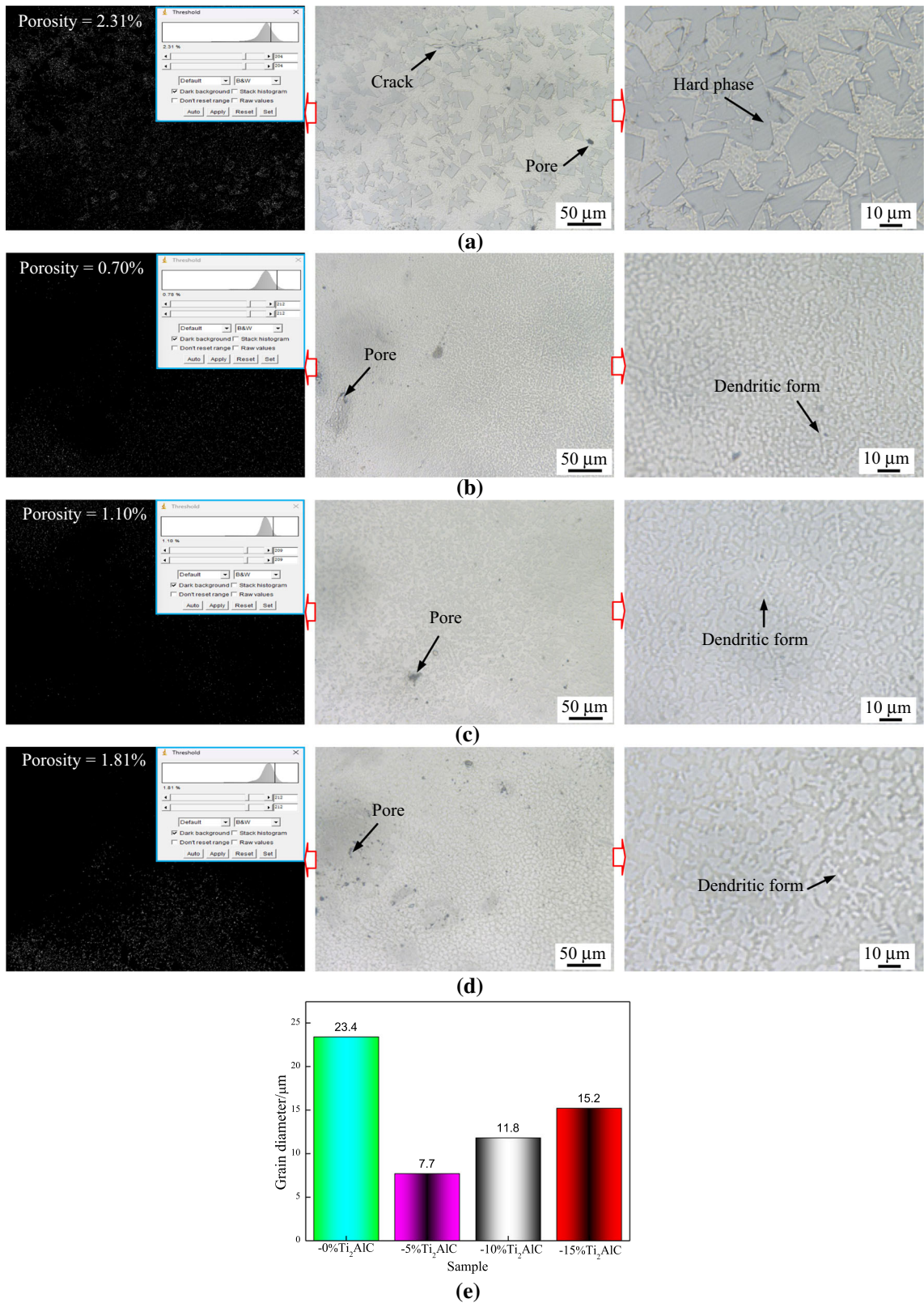


Fig. 2—OM images and porosity of WC10Co4Cr-0 pct Ti₂AlC (a) -5 pct Ti₂AlC (b), -10 pct Ti₂AlC (c) and -15 pct Ti₂AlC (d) coating surfaces and average grain diameters (e).

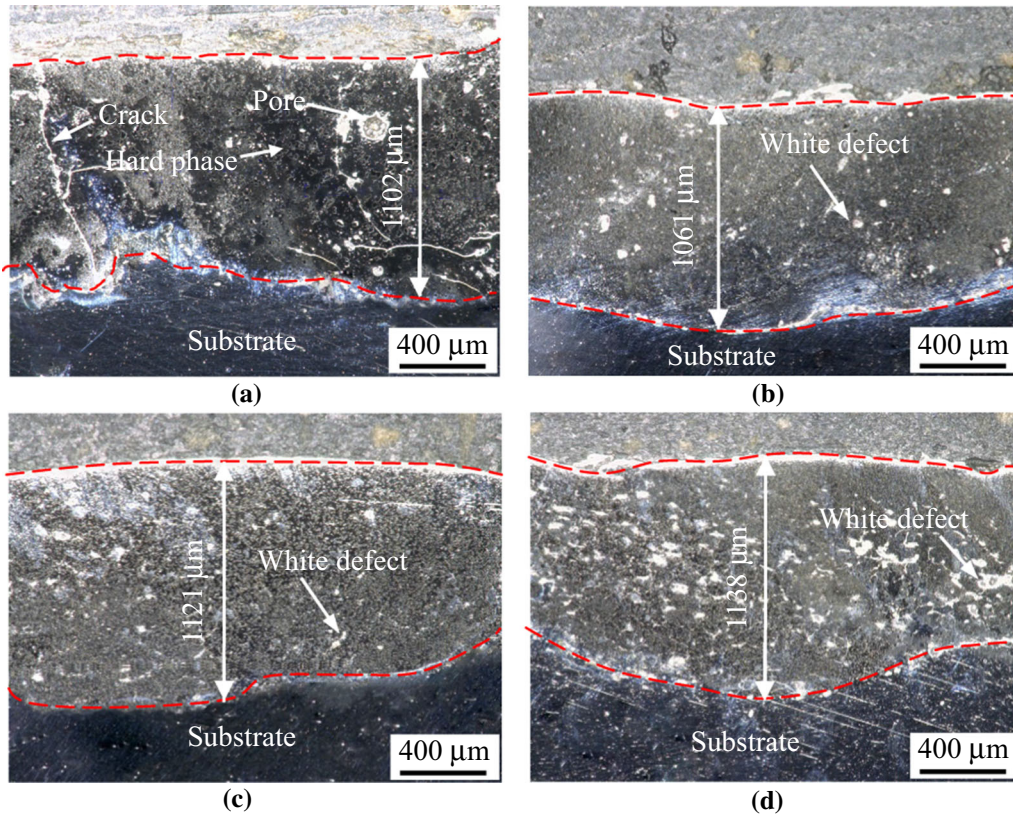


Fig. 3—OM images of WC-10Co4Cr-0 pct Ti₂AlC (a), -5 pct Ti₂AlC (b), -10 pct Ti₂AlC (c), and -15 pct Ti₂AlC (d) coating cross-sections.

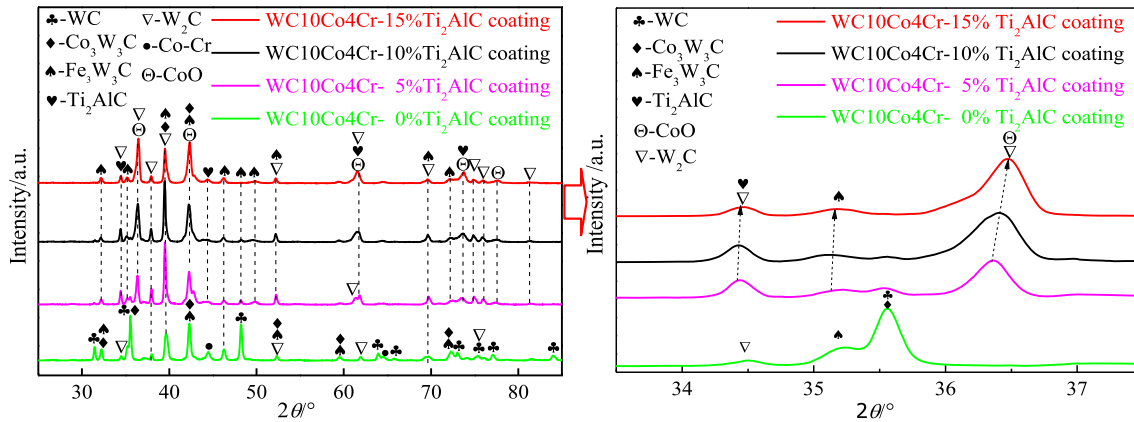


Fig. 4—XRD analysis of WC10Co4Cr-*x*Ti₂AlC coatings.



C. Hardness Distributions

Figure 5(a) shows the hardness distributions of WC10Co4Cr-*x*Ti₂AlC coating surfaces. The hardness of WC10Co4Cr-0 pct Ti₂AlC coating was 1156 ± 57 HV_{0.5}, showing that the coating exhibited higher

hardness than that of a substrate (~ 435 HV_{0.5}). The hardness of WC10Co4Cr-5, -10, and -15 pct Ti₂AlC coatings was 1514 ± 75 , 1423 ± 71 , and 1354 ± 67 HV_{0.5}, respectively, which was increased compared with the WC10Co4Cr-0 pct Ti₂AlC coating surface by 30.6, 23.1, and 17.1 pct, respectively, showing that the addition of Ti₂AlC had the positive effect on the hardness improvement.

Figure 5(b) shows the hardness distributions of WC10Co4Cr-*x*Ti₂AlC coating cross-sections. The hardness of WC10Co4Cr-*x*Ti₂AlC coating cross-sections was greater compared with the WC10Co4Cr-0 pct

Ti₂AlC coating cross-section, and the hardness from the coating surface to the substrate was slowly decreased, indicating that the metallurgical bonding was formed on heat affected zone.^[30,32] Moreover, the grain sizes of WC10Co4Cr-xTi₂AlC coating were refined by the addition of Ti₂AlC, which further enhanced the coating hardness.^[36]

D. Friction-Wear Properties

1. COFs and wear rates

Figure 6(a) shows the COFs of WC10Co4Cr-xTi₂AlC coatings vs. sliding time, in which the wear process consisted of running-in (RI) and steady-wear (SW) periods. All the COF curves exhibited intense fluctuation in the RI period, and the limited contact points between the coatings and the friction-pairs and surface roughness led to changes in COF curves^[37,38]. After the wear entered the SW period, the prominent contact points on the coating surfaces were worn away, and the COFs became stable. The average COFs of WC10Co4Cr-5, -10, and -15 pct Ti₂AlC coatings were 0.419, 0.591, and 0.738, respectively, which were lower than that of WC10Co4Cr-0 pct Ti₂AlC coating (0.828). In this case, the appropriate Ti₂AlC mass fraction played the role of friction reduction, and the wear

resistance of WC10Co4Cr-xTi₂AlC coatings was also enhanced by the addition of Ti₂AlC. This was because the increased hardness led to improved wear resistance, which was analyzed by the following wear rate.

Figure 6(b) shows the profile curves of wear tracks on the WC10Co4Cr-xTi₂AlC coatings. The depths of wear tracks on the WC10Co4Cr-5 pct Ti₂AlC, -10 pct Ti₂AlC, and -15 pct Ti₂AlC coatings were 6.113, 8.065, and 9.924 μm, respectively, which was lower than 11.969 μm of WC10Co4Cr-0 pct Ti₂AlC coating. In this case, the hardness had a contribution to the improvement of wear resistance. The WC10Co4Cr-5 pct Ti₂AlC coating had the smallest depth and width of wear track compared with the other coating, exhibiting the best wear resistance among the four kinds of coatings.

Figure 6(c) shows the wear rates of WC10Co4Cr-xTi₂AlC coatings. The wear rates of WC10Co4Cr-5 pct Ti₂AlC, -10 pct Ti₂AlC, and -15 pct Ti₂AlC coatings calculated from Eq. [1] were 22.71, 34.05, and 39.33 μm³ N⁻¹ mm⁻¹, respectively, which were lower than 55.85 μm³ N⁻¹ mm⁻¹ of WC10Co4Cr-0 pct Ti₂AlC coating. In this case, the wear rates of WC10Co4Cr-5 pct Ti₂AlC, -10 pct Ti₂AlC, and -15 pct Ti₂AlC reduced compared with the WC10Co4Cr-0 pct Ti₂AlC coating by 59.34, 39.03, and 29.60 pct, respectively, showing that the wear resistance of

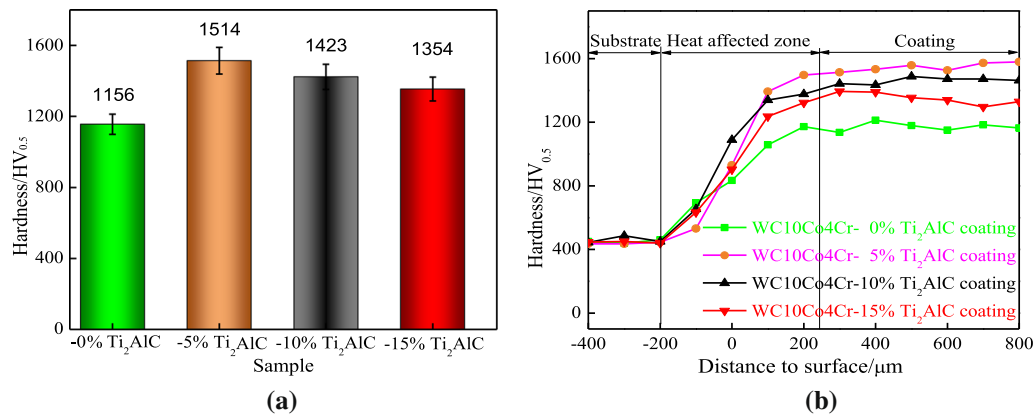


Fig. 5—Hardness distributions of WC10Co4Cr-xTi₂AlC coating surfaces (a) and cross-sections (b).

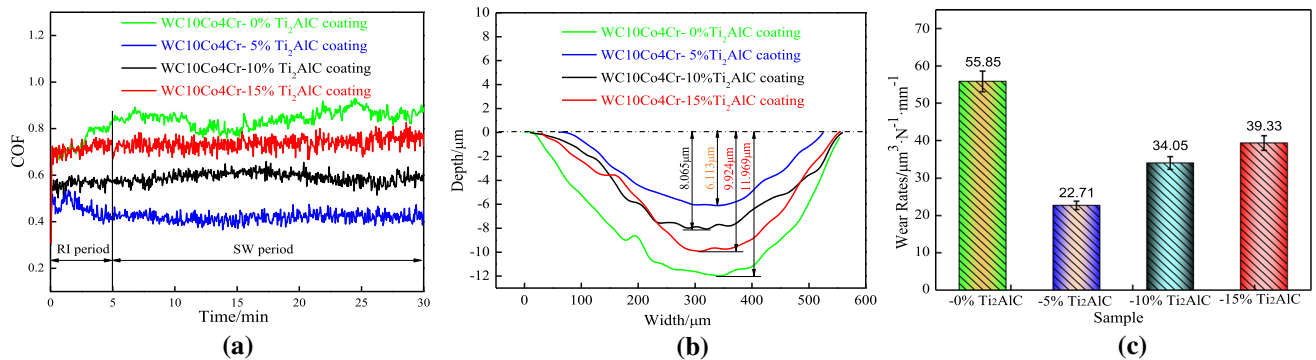


Fig. 6—COFs vs sliding time (a), profiles of wear tracks (b) and wear rates (c) of WC10Co4Cr-xTi₂AlC coatings.

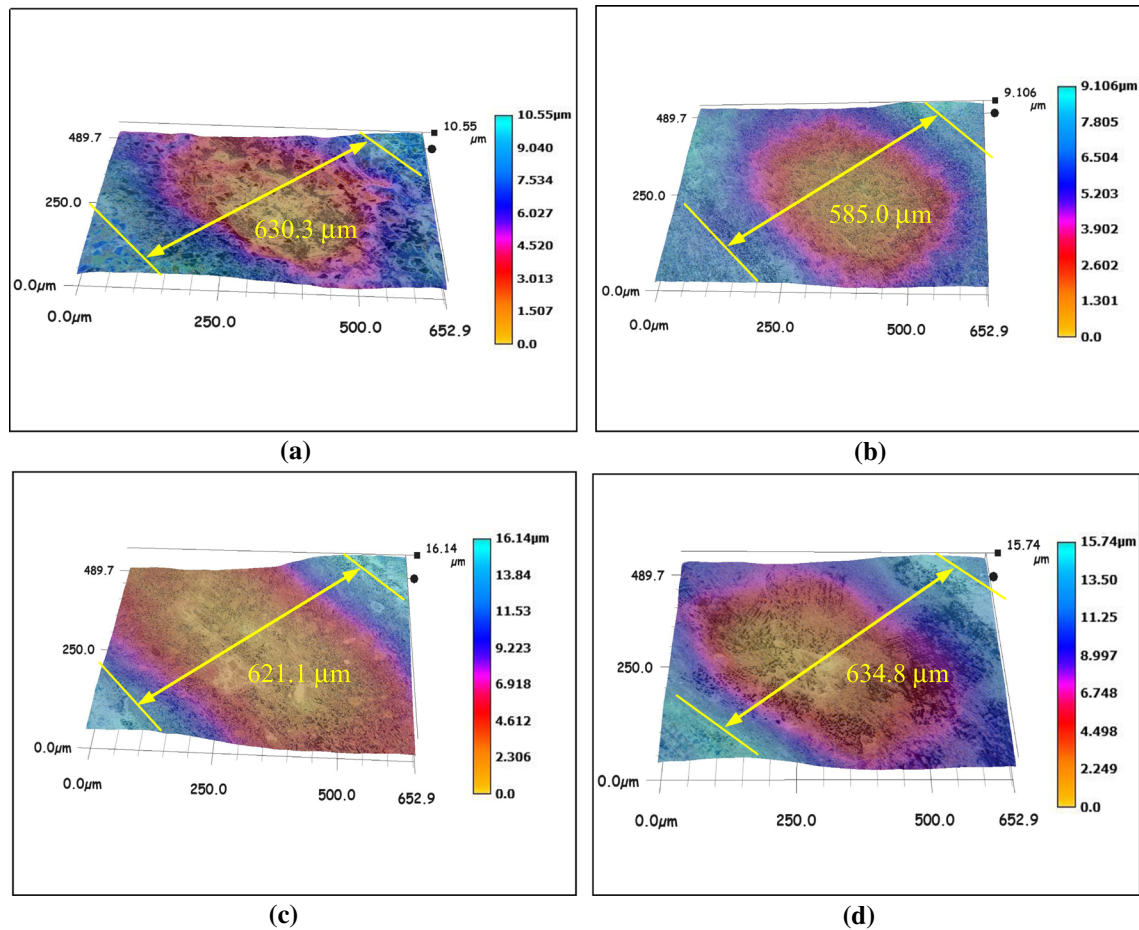


Fig. 7—3D images of wear tracks on WC10Co4Cr-0 pct Ti₂AlC (a), -5 pct Ti₂AlC (b), -10 pct Ti₂AlC (c), and -15 pct Ti₂AlC (d) coatings.

WC10Co4Cr-5 pct Ti₂AlC coating was the most obvious.

2. 3D images of wear tracks

Figures 7(a) through (d) shows the 3D profiles of wear tracks on the WC10Co4Cr-*x*Ti₂AlC coatings. The widths of wear tracks on the WC10Co4Cr-0 pct Ti₂AlC, -5 pct Ti₂AlC, -10 pct Ti₂AlC, and -15 pct Ti₂AlC coatings were 630.3, 585.0, 621.1, and 634.8 μm, respectively, indicating that the width of wear track on the WC10Co4Cr-5 pct Ti₂AlC coating was the smallest. Moreover, the wear track on the WC10Co4Cr-0 pct Ti₂AlC coating had a large color variation, in which the pores and cracks were caused by the worn chips (Figure 7(a)). The widths of wear tracks on the WC10Co4Cr-*x*Ti₂AlC coatings were increased with the Ti₂AlC mass fraction (Figures 7(b) through (d)), which was because the excessive Ti₂AlC had little strengthening effort for the WC10Co4Cr-*x*Ti₂AlC coatings.

3. Morphologies of wear tracks

Figure 8(a) shows the morphologies of the wear track on the WC10Co4Cr-0 pct Ti₂AlC coating. Under the action of normal load, the wear track exhibited bad wear resistance, and slight ploughs were observed on the

wear track; while other regions were cut, which resulted in the formation of pores.^[39] The continuously normal load produced some defects such as debris and cracks, which were adhered on the wear track to participate in the wear process. The hard phases on the wear track suffered excessive stress to form cracks and further developed into voids and large delamination.^[40] This was attributed to the high brittleness of WC, which caused the wear resistances of WC10Co4Cr-0 pct Ti₂AlC coating to deteriorate.

Figure 8(b) shows the morphologies of the wear track on the WC10Co4Cr-5 pct Ti₂AlC coating. Compared with the WC10Co4Cr-0 pct Ti₂AlC coating, the presence of debris, pores and scratches were significantly reduced, showing better wear resistance. The hard phases became more round and smooth by the addition of Ti₂AlC, which was because the sharp edges of hard phases became smooth to achieve a more uniform distribution by the addition of Ti₂AlC.

Figures 8(c) and (d) shows the morphologies of wear tracks on the WC10Co4Cr-10 pct Ti₂AlC and -15 pct Ti₂AlC coatings. The wear resistance deteriorated with the increase of Ti₂AlC mass fraction, and the presence of pores on the wear tracks also increased and some flakey debris were attached to the wear tracks. With the continuation of the wear process, the wear debris

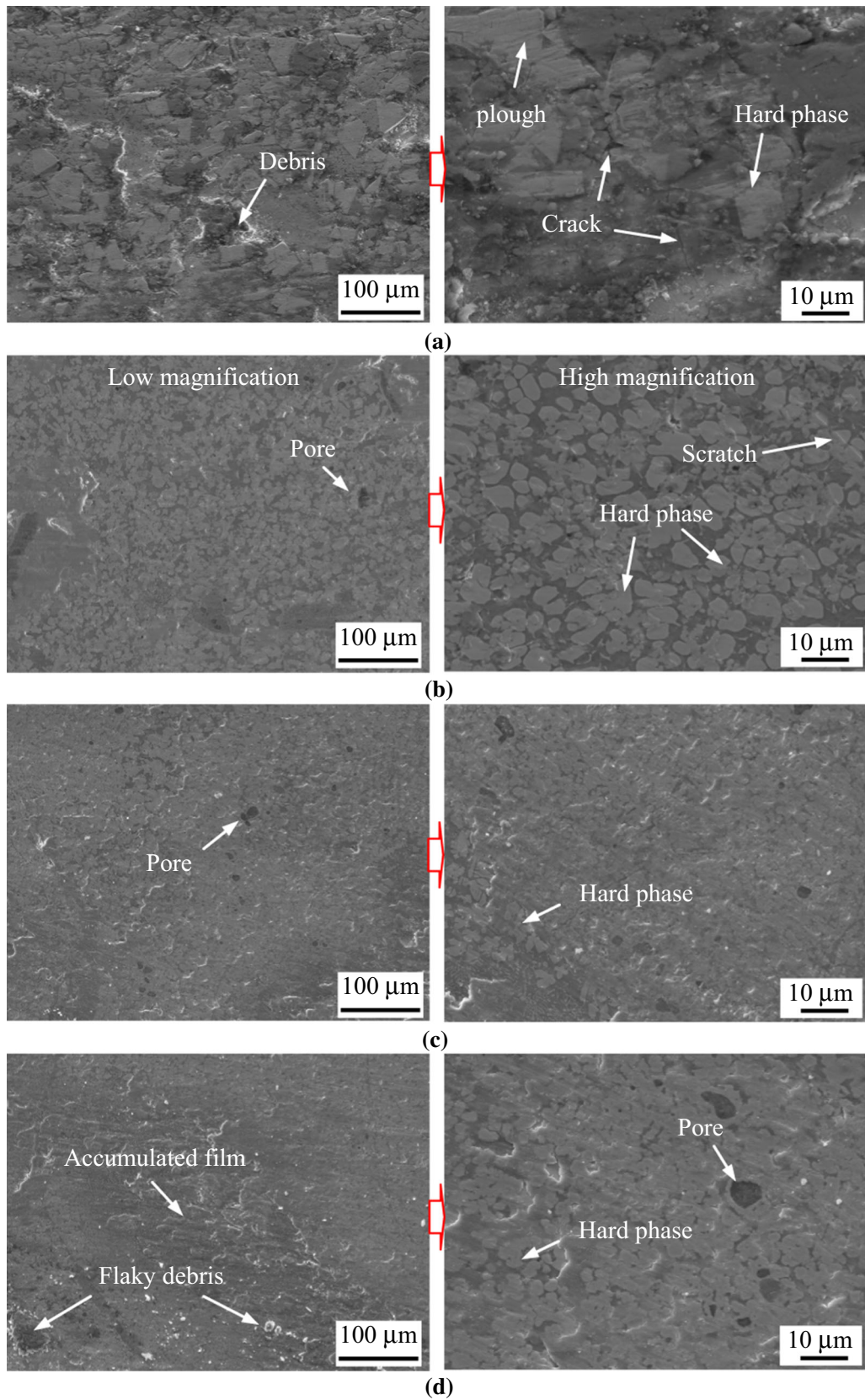


Fig. 8—SEM images of wear tracks on WC10Co4Cr-0 pct Ti₂AlC (a), -5 pct Ti₂AlC (b), -10 pct Ti₂AlC (c), and -15 pct Ti₂AlC (d) coatings.

accumulated on the wear tracks and formed the special tribofilm,^[41] which had a certain effect of wear resistance in the friction process.

In this case, compared with the WC10Co4Cr-0 pct Ti₂AlC coating, the WC10Co4Cr-*x*Ti₂AlC coatings exhibited better wear resistance. However, as the Ti₂AlC mass fraction increased, the wear resistance of WC10Co4Cr-*x*Ti₂AlC coatings decreased, indicating that the appropriate Ti₂AlC mass fraction improved their wear resistance.

4. Mapping analysis of wear tracks

Figure 9(a) shows the mapping analysis of the wear track on the WC10Co4Cr-0 pct Ti₂AlC coating, in which the W, C, Co, Cr, Ti, Al, Fe, Si, and O were detected on the wear track. The debris was observed on the wear track, and there were lower W and Si mass fractions on the debris region. The uneven distributions

of C and Co on the wear track indicated that the element segregations occurred during the LC process^[39,42]; while the appearance of Si originated from the material transfer of friction-pair.

Figure 9(b) shows the mapping analysis of the wear track on the WC10Co4Cr-5 pct Ti₂AlC coating. The wear track exhibited the uniform distributions of elements, and there were no obvious atom-rich or -poor regions except for the C element. The black spots indicated that the regions were enriched on the carbon atoms, which were highlighted in the brighter color. The debris revealed a high content of O, which was attributed to the formation of oxides.^[43]

Figure 9(c) shows the mapping analysis of the wear track on the WC10Co4Cr-10 pct Ti₂AlC coating. As the Ti₂AlC mass fraction increased, the distribution of other elements remained uniform except for the Ti and Al. This was the result that the excessive Ti₂AlC caused

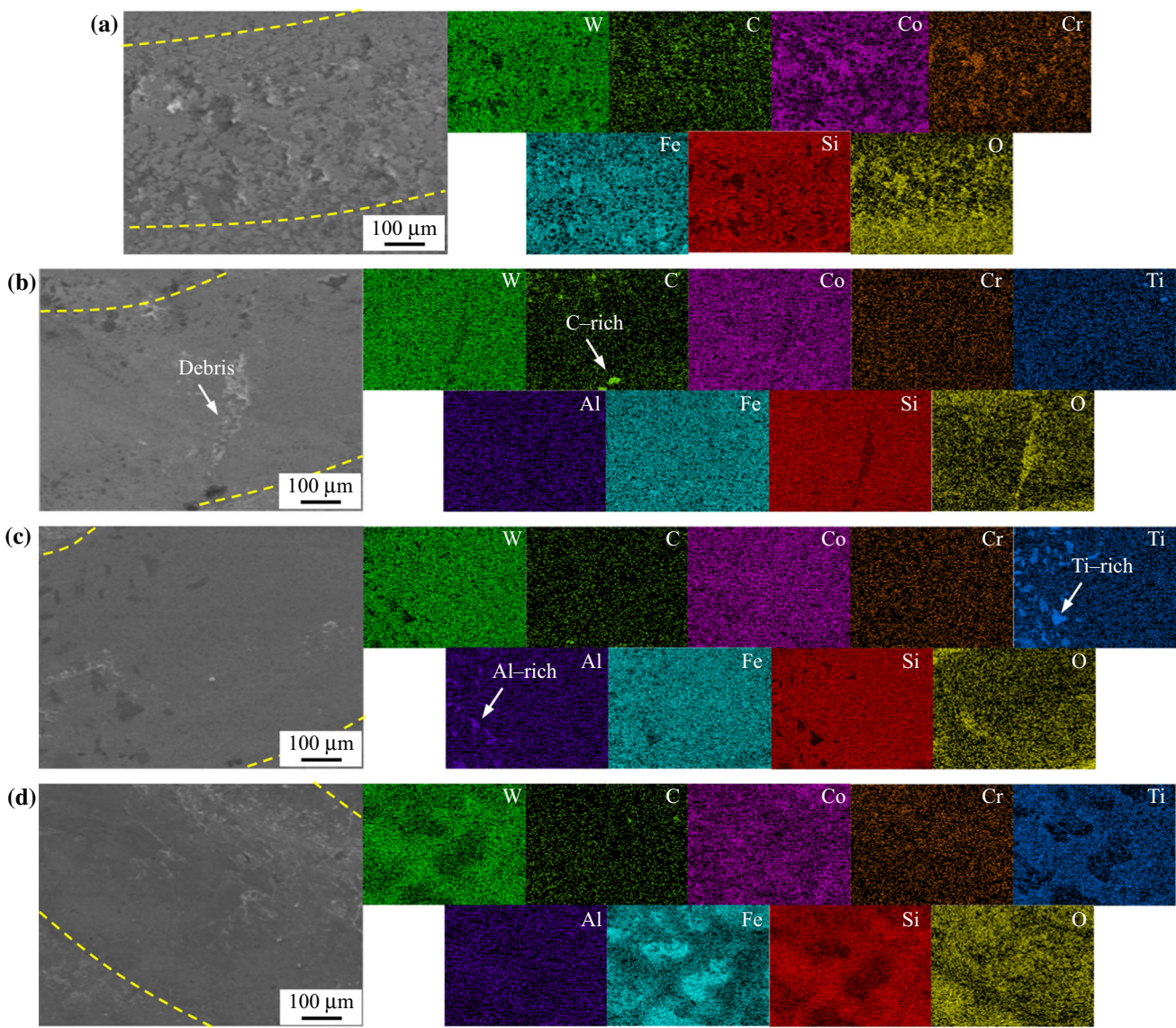
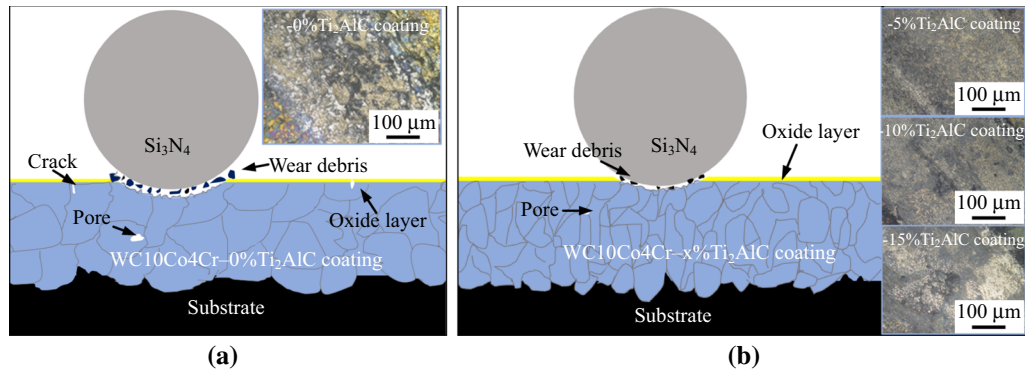


Fig. 9—Mapping analysis of wear tracks on WC10Co4Cr-0 pct Ti₂AlC (a), -5 pct Ti₂AlC (b), -10 pct Ti₂AlC (c), and -15 pct Ti₂AlC (d) coatings.

Table I. Mass Fractions of Chemical Elements on Wear Tracks of WC10Co4Cr-*x*Ti₂AlC Coatings /Pct

Sample	C	W	Co	Cr	Ti	Al	Fe	Si	O
WC10Co4Cr-0 pct Ti ₂ AlC	11.03	50.08	6.12	0.84	—	—	10.73	4.98	16.22
WC10Co4Cr-5 pct Ti ₂ AlC	8.09	53.12	7.99	0.07	1.52	0.55	13.28	2.11	13.27
WC10Co4Cr-10 pct Ti ₂ AlC	6.01	50.38	7.57	0.04	2.45	1.25	16.61	2.38	13.31
WC10Co4Cr-15 pct Ti ₂ AlC	4.59	47.39	7.30	0.14	4.57	0.99	17.51	3.95	13.56

**Fig. 10—Wear models of WC10Co4Cr-0 pct Ti₂AlC (a) and -5 pct Ti₂AlC, -10 pct Ti₂AlC and -15 pct Ti₂AlC coatings (b).**

inadequate decomposition during the LC process. The distributions of W, Fe and Si were unchanged, which were not reacted with the Ti₂AlC.

Figure 9(d) shows the mapping analysis of the wear track on the WC10Co4Cr-15 pct Ti₂AlC coating. The distributions of W, Ti, and Si were similar on the WC10Co4Cr-15 pct Ti₂AlC coating; while the Fe was noticeably decreased on the regions. The oxide layer was worn away by the friction-pair, and the O was reduced on the wear track. Moreover, the oxide layer played a protective role during the wear process, and the rest elements exhibited a uniform distribution, which was similar to the other two kinds of coatings.

The results of the mapping analysis (Figure 9) are listed in Table I. The O mass fraction on the wear track of WC10Co4Cr-0 pct Ti₂AlC coating counted for 16.22 pct; while those on the WC10Co4Cr-5 pct Ti₂AlC, -10 pct Ti₂AlC, -15 pct Ti₂AlC coatings accounted for 13.27, 13.31, and 13.56 pct, respectively. As a result, the mass of Ti₂AlC had little impact on the oxidative wear.

E. Wear Mechanism

Figure 10(a) shows the wear model of WC10Co4Cr-0 pct Ti₂AlC coating. The SEM and mapping images (Figures 8, 9) and EDS results (Table I) indicated that oxidative wear was presented on the wear track, and the oxide layer was removed by the friction-pair, which played a certain protection for the coating.^[44] The normal load acted on the wear track, which produced microcracks and pores. With the continuation of the

wear process, the contact area of the friction-pair led to the generation of abrasion particles and scratches. The wear debris and abrasion particles broke away from the wear track, and the plastic deformation zone and pits occurred (Figures 8(a)), which caused a substantial loss of wear volume.^[45] Therefore, the wear mechanism of WC10Co4Cr-0 pct Ti₂AlC coating was abrasive wear, fatigue wear, and oxidative wear.

Figure 10(b) shows the wear model of WC10Co4Cr-*x*Ti₂AlC coatings. The plastic deformation of the wear track was reduced by the addition of Ti₂AlC, and the wear defects were mainly slight scratches and shallow spalling.^[40] Furthermore, the COFs and wear rates of WC10Co4Cr-*x*Ti₂AlC coatings were lower than the WC10Co4Cr-0 pct Ti₂AlC coating (Figure 6), indicating that the wear resistance of WC10Co4Cr-5 pct Ti₂AlC coatings was improved by the addition of Ti₂AlC, in which the Ti₂AlC was dispersed in the grain boundaries and eutectic regions. Moreover, the CoCr binder was refined by the addition of Ti₂AlC, and the wear rates were decreased by the grain refinement effect (Figure 2(e)). In this case, the Ti₂AlC hindered the elastic deformation by the improvement of hardness, which weakened the cutting effect of WC10Co4Cr-*x*Ti₂AlC coating by the friction-pair, showing that the wear resistance was increased by the addition of Ti₂AlC. Therefore, the wear mechanism of WC10Co4Cr-*x*Ti₂AlC coating was abrasive wear, oxidative wear and slight adhesive wear, which was attributed to the lubrication effect and hardness improvement by the addition of Ti₂AlC.

IV. CONCLUSIONS

- (1) The WC10Co4Cr- x Ti₂AlC coatings are composed of WC, W₂C, Co₃W₃C, Fe₃W₃C, Co-Cr, Ti₂AlC and CoO phases, and the grains are refined by the addition of Ti₂AlC, which further reduce the coating porosity. Moreover, the appropriate Ti₂AlC mass fraction improves the coatings hardness.
- (2) The average COFs of WC10Co4Cr-5 pct Ti₂AlC, -10 pct Ti₂AlC and -15 pct Ti₂AlC coatings are 0.419, 0.591, and 0.738, respectively, and the corresponding wear rates are 22.71, 34.05, and 39.33 $\mu\text{m}^3 \text{N}^{-1} \text{mm}^{-1}$, respectively, showing that the WC10Co4Cr-5 pct Ti₂AlC coating exhibits the best friction reduction and wear resistance.
- (3) The wear mechanism of WC10Co4Cr- x Ti₂AlC coating is abrasive wear, oxidative wear and slight adhesive wear, which is attributed to the lubrication and refinement strengthening effects of Ti₂AlC phase.

CONFLICT OF INTEREST

On behalf of all authors, the corresponding author states that there is no conflict of interest.

REFERENCES

1. J. Zhu, Z. Zhang, and J. Xie: *Mater. Sci. Eng. A*, 2019, vol. 752, pp. 101–14. <https://doi.org/10.1016/j.msea.2019.02.085>.
2. B. Breidenstein, B. Denkena, P. Wolters, M. Keitel, W. Tillmann, D. Stangier, and N.F. Lopes Dias: *Mater. Today Sustain.*, 2023, vol. 24, p. 100507. <https://doi.org/10.1016/j.mtsust.2023.100507>.
3. H. Li, D. Xiang, Y. Cao, S. Zhao, and G. Tu: *Ceram. Int.*, 2017, vol. 43(17), pp. 14726–31. <https://doi.org/10.1016/j.ceramint.2017.07.204>.
4. H. Yang, X. Wu, G. Cao, and Z. Yang: *Surf. Coat. Technol.*, 2016, vol. 307, pp. 506–16. <https://doi.org/10.1016/j.surfcoat.2016.09.029>.
5. D. Wang, L. Zhang, X. Luo, and C. Li: *Corros. Sci.*, 2022, vol. 209, p. 110800. <https://doi.org/10.1016/j.corsci.2022.110800>.
6. S. Sun, J. Wang, J. Xu, X. Cheng, C. Jing, Z. Chen, H. Ru, Y. Liu, and J. Jiao: *Mater. Today Commun.*, 2023, vol. 37, p. 106939. <https://doi.org/10.1016/j.mtcomm.2023.106939>.
7. L. Kang, F. Chen, B. Wu, X. Liu, and H. Ge: *J. Constr. Steel Res.*, 2022, vol. 199, p. 107603. <https://doi.org/10.1016/j.jcsr.2022.107603>.
8. J. Jiang, W. Hou, X. Feng, and Y. Shen: *Surf. Coat. Technol.*, 2023, vol. 464, p. 129577. <https://doi.org/10.1016/j.surfcoat.2023.129577>.
9. C. Chen, A. Feng, Y. Wei, Y. Wang, X. Pan, and X. Song: *Mater. Lett.*, 2023, vol. 337, p. 133939. <https://doi.org/10.1016/j.matlet.2023.133939>.
10. Y. Zhu, H. Zhou, Z. Chen, Z. Wang, F. He, and C. Xu: *Micro-machines*, 2022, vol. 13(5), p. 653. <https://doi.org/10.3390/mi13050653>.
11. J. Ma, Y. Duan, W. Chen, Q. Li, J. Guo, X. Cao, H. Tan, J. Cheng, Q. Sun, and J. Yang: *Wear*, 2023, vol. 530–31, p. 205031. <https://doi.org/10.1016/j.wear.2023.205031>.
12. J. Liu, S. Yang, W. Xia, X. Jiang, and C. Gui: *J. Alloy. Compd.*, 2016, vol. 654, pp. 63–70. <https://doi.org/10.1016/j.jallcom.2015.09.130>.
13. H. Wang, M. Gee, Q. Qiu, H. Zhang, X. Liu, H. Nie, X. Song, and Z. Nie: *J. Mater. Sci. Technol.*, 2019, vol. 35(11), pp. 2435–46. <https://doi.org/10.1016/j.jmst.2019.07.016>.
14. Z. Wang, M. Tan, J. Wang, J. Zeng, F. Zhao, X. Xiao, S. Xu, B. Liu, L. Gong, Q. Sui, R. Zhang, B. Han, and J. Liu: *J. Alloy. Compd.*, 2021, vol. 878, p. 160127. <https://doi.org/10.1016/j.jallcom.2021.160127>.
15. M.W. Barsoum: *Prog. Solid State Ch.*, 2000, vol. 28(14), pp. 201–81. [https://doi.org/10.1016/S0079-6786\(00\)00006-6](https://doi.org/10.1016/S0079-6786(00)00006-6).
16. E. Hugon, O. Rapaud, R. Lucas, and T. Chotard: *Open Ceram.*, 2023, vol. 15, p. 100398. <https://doi.org/10.1016/j.oceram.2023.100398>.
17. H. Xiao, S. Zhao, Q. Liu, Y. Li, S. Zhao, F. Luo, Y. Wang, Q. Huang, and C. Wang: *Acta Mater.*, 2023, vol. 248, p. 118783. <https://doi.org/10.1016/j.actamat.2023.118783>.
18. H. Chen, Y. Du, D. Wang, C. Zhang, G. Yang, B. Liu, Y. Gao, and S. Shi: *Ceram. Int.*, 2018, vol. 44(18), pp. 22520–28. <https://doi.org/10.1016/j.ceramint.2018.09.023>.
19. G. Song, Y. Pei, W. Sloof, S. Li, J. Hosson, and S. Zwaag: *Scripta Mater.*, 2008, vol. 58(1), pp. 13–16. <https://doi.org/10.1016/j.scriptamat.2007.09.006>.
20. S. Li, G. Song, K. Kwakernaak, S. Zwaag, and W. Sloof: *J. Eur. Ceram. Soc.*, 2012, vol. 21(8), pp. 1813–20. <https://doi.org/10.1016/j.jeurceramsoc.2012.01.017>.
21. S. Hua, M. Pang, F. Ji, J. Chen, and G. Liu: *Mater. Today Commun.*, 2023, vol. 34, p. 105165. <https://doi.org/10.1016/j.mtcomm.2022.105165>.
22. C. Jiang, J. Zhang, Y. Chen, Z. Hou, Q. Zhao, Y. Li, L. Zhu, F. Zhang, and Y. Zhao: *Int. J. Refract Metal Hard Mater.*, 2022, vol. 107, p. 105902. <https://doi.org/10.1016/j.ijrmhm.2022.105902>.
23. P. Tatarko, M. Kašiarová, Z. Chlup, J. Dusza, P. Šajgalik, and I. Vávra: *Wear*, 2013, vol. 300(1–2), pp. 155–62. <https://doi.org/10.1016/j.wear.2013.01.030>.
24. W. Shao, Y. Zhou, L. Zhou, L. Rao, X. Xing, Z. Shi, and Q. Yang: *Mater. Design*, 2021, vol. 211, p. 110133. <https://doi.org/10.1016/j.matdes.2021.110133>.
25. L. Zhang, C. Wang, X. Huang, R. Nie, J. Zhu, and X. Yan: *Int. J. Refract Metal Hard Mater.*, 2023, vol. 115, p. 106309. <https://doi.org/10.1016/j.ijrmhm.2023.106309>.
26. G. Lee, T. Kim, W. Sloof, and K. Lee: *Ceram. Int.*, 2021, vol. 47(16), pp. 22478–86. <https://doi.org/10.1016/j.ceramint.2021.04.257>.
27. V. Katranidis, S. Gu, B. Allcock, and S. Kamnis: *Surf. Coat. Technol.*, 2017, vol. 311, pp. 206–15. <https://doi.org/10.1016/j.surfcoat.2017.01.015>.
28. Z. Liu, J. Shi, C. He, F. Wang, and D. Kong: *Int. J. Appl. Ceram. Technol.*, 2023, vol. 20(5), pp. 2847–59. <https://doi.org/10.1111/ijac.14403>.
29. A. Khorram, A. Jamaloei, and R. Sepehrnia: *Optik*, 2022, vol. 264, p. 169407. <https://doi.org/10.1016/j.ijleo.2022.169407>.
30. G. Cui, B. Han, J. Zhao, and M. Li: *Tribol. Int.*, 2019, vol. 134, pp. 36–49. <https://doi.org/10.1016/j.triboint.2019.01.019>.
31. A. Sharma and D. Gupta: *Appl. Surf. Sci.*, 2012, vol. 258(15), pp. 5583–92. <https://doi.org/10.1016/j.apsusc.2012.02.019>.
32. D. Ravnikar, N. Dahotre, and J. Grum: *Appl. Surf. Sci.*, 2013, vol. 282, pp. 914–22. <https://doi.org/10.1016/j.apsusc.2013.06.089>.
33. T. Sudaprasert, P. Shipway, and D. McCartney: *Wear*, 2003, vol. 255(7–12), pp. 943–49. [https://doi.org/10.1016/S0043-1648\(03\)00293-X](https://doi.org/10.1016/S0043-1648(03)00293-X).
34. Y. Zhou, X. Liu, J. Kang, W. Yue, W. Qin, G. Ma, Z. Fu, L. Zhu, D. She, H. Wang, J. Liang, W. Weng, and C. Wang: *Eng. Fail. Anal.*, 2020, vol. 109, p. 104338. <https://doi.org/10.1016/j.engfailanal.2019.104338>.
35. D. Stewart, P. Shipway, and D. McCartney: *Acta Mater.*, 2000, vol. 48(7), pp. 1593–1604. [https://doi.org/10.1016/S1359-6454\(99\)00440-1](https://doi.org/10.1016/S1359-6454(99)00440-1).
36. H. Jiang, F. Su, Y. Yang, D. Zhang, Y. Hong, H. Cui, F. Min, C. Wang, G. Li, and J. Zhang: *Int. J. Refract Metal Hard Mater.*, 2023, vol. 115, p. 106303. <https://doi.org/10.1016/j.ijrmhm.2023.106303>.

37. M. Yin, Y. Shao, X. Kang, J. Long, and X. Zhang: *Tribol. Int.*, 2023, vol. 177, p. 107975. <https://doi.org/10.1016/j.triboint.2022.107975>.
38. L. Zhao, Z. Zhang, B. Wang, S. Xu, and C. Si: *Mater. Lett.*, 2022, vol. 328, p. 133203. <https://doi.org/10.1016/j.matlet.2022.133203>.
39. Y. Yu, Y. Wu, S. Hong, J. Cheng, S. Zhu, and H. Li: *Ceram. Int.*, 2023, vol. 49(17–B), pp. 28560–70. <https://doi.org/10.1016/j.ceramint.2023.06.148>.
40. Y. Chen, D. Wang, W. Wang, Y. Liu, Y. Sato, T. Yamaguchi, Y. Chen, and C. Wang: *Surf. Coat. Technol.*, 2021, vol. 422, pp. 127–493. <https://doi.org/10.1016/j.surfcoat.2021.127493>.
41. V. Kumar, R. Verma, and S. Shrivastava: *Mater. Today Proc.*, 2023, <https://doi.org/10.1016/j.matpr.2023.08.044>.
42. H. Wang, H. Lu, X. Song, X. Yan, X. Liu, and Z. Nie: *Corros. Sci.*, 2019, vol. 147, pp. 372–83. <https://doi.org/10.1016/j.corsci.2018.11.028>.
43. R. Khuengpukheiw, A. Wisitsoraat, and C. Saikaew: *Wear*, 2021, vol. 484–485, p. 203699. <https://doi.org/10.1016/j.wear.2021.203699>.
44. Q. Cao, L. Fan, H. Chen, Y. Hou, L. Dong, and Z. Ni: *Tribol. Int.*, 2022, vol. 176, p. 107939. <https://doi.org/10.1016/j.triboint.2022.107939>.
45. G. Chen, X. Liu, F. Zhang, Q. Liu, H. Ou, and S. Zhang: *Surf. Coat. Technol.*, 2023, vol. 472, p. 129930. <https://doi.org/10.1016/j.surfcoat.2023.129930>.

Publisher's Note Springer Nature remains neutral with regard to jurisdictional claims in published maps and institutional affiliations.

Springer Nature or its licensor (e.g. a society or other partner) holds exclusive rights to this article under a publishing agreement with the author(s) or other rightsholder(s); author self-archiving of the accepted manuscript version of this article is solely governed by the terms of such publishing agreement and applicable law.